Composites Part B 237 (2022) 109856

Contents lists available at ScienceDirect

Composites Part B

journal homepage: www.elsevier.com/locate/compositesb

Hierarchically porous N-doped C nanofibers comprising TiO_2 quantum dots and ZIF-8-derived hollow C nanocages as ultralight interlayer for stable Li–S batteries

Young Hoe Seon, Rakesh Saroha, Jung Sang Cho *

Department of Engineering Chemistry, Chungbuk National University, Chungbuk, 361-763, Republic of Korea

ARTICLE INFO

Keywords:
Li–S batteries
Electrospinning
N-doped C fibers
Metal-oxide quantum dots
Functional interlayer

ABSTRACT

Hierarchically porous nanofibers comprising TiO_2 quantum dots and metal-organic-framework-derived hollow N-doped C nanocages (HNCs), abbreviated as P-N-C@TiO_2/HNC NFs, have been introduced as ultra-lightweight multifunctional interlayers for stable Li–S batteries (LSBs). The hierarchically porous and highly conductive N–C nanofiber framework provides numerous conductive channels for rapid ionic/electronic transfer and support fast redox processes in addition to an efficient electrolyte percolation. Further, the presence of well-grafted polar TiO_2 quantum dots ensures an efficient trapping and reuse of the lithium polysulfide species thus prohibits their migration toward the Li anode leading to high active-material utilization. Benefitting from these structural merits, the Li–S cells utilizing a high effective sulfur content (~61 wt%) electrode and P-N-C@TiO_2/HNC-NF-coated separator exhibits satisfactory rate and cycling performance (590 mA h g^{-1} after 500 cycles at 0.1C with an average capacity fading of only 0.11%). The combined strategy of developing a porous and highly conductive N–C framework comprising well-embedded polar TiO_2 quantum dots reported in this work will provide valuable insights to the synthesis of advanced functional interlayers suitable for applications in various energy storage systems.

1. Introduction

Li–S batteries (LSBs) are now considered as a possible alternative to state-of-the-art Li-ion batteries as the latter have approached their theoretical capacity [1,2]. LSBs provide a high energy density (2600 W h kg^{-1}), high theoretical specific discharge capacity (1675 mA h g^{-1}), and nominal operating voltage of 2.1 V vs. Li^+/Li. They are environment-friendly owing to the low toxicity of sulfur and are economic owing to the use of earth-abundant sulfur [3–8]. However, several fundamental drawbacks have hindered their commercial application, which mainly include the low conductivity of sulfur ($\sigma = 10^{-30}$ S cm^{-1}) and its discharge products (Li_2S; $\sigma = 10^{-13}$ S cm^{-1}), formation and diffusion of intermediate lithium polysulfides (Li_2S_x; $8 \geq x \geq 4$) during the redox processes, severe volume variation due to the density difference between S and Li_2S, and instability of the Li anode [9–12]. Consequently, LSBs display inferior electrochemical performance with low-rate capabilities, unstable cycling performance, and low Coulombic efficiencies [13–17].

Several strategies have been developed to overcome these problems, including the synthesis of carbon–sulfur nanocomposites [18–22], the physical and chemical anchoring of polysulfides through the use of various polar oxide/selenide/carbide/sulfide nanomaterials along with carbon [23–37], electrolyte modification [38,39], and Li anode protection [40,41]. Another interesting strategy reported by various research groups over the world is the introduction of a porous and highly conductive interlayer consisting of mainly carbon and metal compounds as nanocomposites in the form of separator coating facing toward the cathode. The non-polar carbon nanostructure used in the interlayer usually has high specific surface area, which channelizes the volume stress during the electrochemical processes and serves as an additional conductive framework. Additionally, the polar metal oxides act as anchoring sites for an efficient polysulfide capture, which inhibits the shuttling effect and hence increases the active-material utilization.

Herein, we propose a multicomponent strategy to synthesize a highly porous and conducting carbon nanostructure comprising well-embedded polar TiO_2 quantum dots and HNCs using an electrospinning technique. The designed nanostructure was then applied to a commercial Celgard 2400 membrane to obtain an ultra-lightweight

* Corresponding author.
E-mail address: jscho@cbnu.ac.kr (J.S. Cho).

https://doi.org/10.1016/j.compositesb.2022.109856
Received 4 February 2022; Received in revised form 19 March 2022; Accepted 26 March 2022
Available online 28 March 2022

multifunctional interlayer suitable for stable LSBs. The hierarchical porous structure was obtained using the combined effect of polystyrene (PS) nanobeads and zeolitic imidazolate framework (ZIF-8) units as pore-forming agents. The decomposition of the PS nanobeads and ZIF-8 polyhedrons during the heat treatment results in a hierarchically porous carbon nanostructure with highly interconnected HNCs. The porous structure ensures sufficient space for an efficient electrolyte percolation, which subsequently allows for a rapid electronic/ionic diffusion and channelizes the severe volume stress that occurs during the redox processes. Similarly, the presence of polar TiO_2 quantum dots guarantees the efficient anchoring of the lithium polysulfide species, mitigating their diffusion toward the Li anode thus resulting in high active-material utilization.

Benefiting from these structural merits, the Li–S cell utilizing functional interlayer and regular sulfur electrodes with a high sulfur content (~61 wt%) exhibits a reasonable rate capability, stable long-term cycling performance, and an overall enhanced electrochemical performance. Therefore, we believe that the synthesis strategy discussed in this paper will open up new possibilities for the development of hierarchically porous and highly conductive nanostructured materials suitable for various energy storage applications.

2. Material and methods

2.1. Chemicals

Analytical-grade chemicals were used without purification for the synthesis of the hierarchically porous nanofibers with well-embedded TiO_2 quantum dots. Polyvinylpyrrolidone (PVP; M_w = 1300000, 98%, Alfa Aesar), titanium (IV) isopropoxide ($Ti(OCH(CH_3)_3)_4$, TTIP; M_w = 284.23, 98%, Junsei), PS nanobeads (φ = 40 nm), 2-methylimidazole ($C_4H_6N_2$; M_w = 82.10, 99%, Acros Organics), and zinc nitrate hexahydrate ($Zn(NO_3)_2{\cdot}6H_2O$; M_w = 297.47, 96.0%, Junsei) were used. The spinning solution was prepared using ethanol (C_2H_5OH; 99.9%, Duksan) as the solvent.

2.2. Synthesis process

Hierarchically porous nanofibers comprising TiO_2 quantum dots and metal-organic-framework-derived hollow N-doped C nanocages (P-N-C@TiO_2/HNC NFs) were synthesized using conventional electrospinning technique and subsequent post-heat-treatment process. ZIF-8 polyhedral crystals were synthesized using a facile solution method, as previously reported [1]. In a typical procedure, 1.0 g of ZIF-8 polyhedrons was dissolved in 10 mL of ethanol using repeated ultrasonication and stirring steps until a milky solution was obtained, following which 5 mL of the PS nanobeads (φ = 40 nm) suspension was added to the former solution. The PS-nanobead suspension was prepared using an emulsion polymerization technique, as reported in previous study, and was used as a pore generator along with the ZIF-8 polyhedrons [42]. The resulting solution was vigorously stirred at room temperature, followed by the addition of TTIP (12 wt% of the ZIF-8) and 1.0 g of PVP. The resulting white colloidal suspension was stirred overnight at an ambient temperature. The obtained spinning solution was loaded into a plastic syringe pump (12 mL capacity) fitted with stainless-steel needle (21-gauge). The solution was fed at a speed of 3 mL h^{-1} onto an aluminum collector attached to a rotating drum (180 rpm). The applied voltage and distance between the needle tip and collector were fixed at 20 kV and 15 cm, respectively. The as-spun PVP/TTIP/ZIF-8/PS composite fibers were stabilized in a hot air oven at 150 °C for 48 h. Subsequently, the fibers were further subjected to heat treatment at 800 °C for 5 h under a flowing N_2 gas atmosphere. The second heat treatment was carried out at 300 °C for 3 h under an ambient atmosphere to obtain the P-N-C@TiO_2/HNC composite NFs. For comparison, samples without TTIP, i.e., porous N-doped carbon network with hollow carbon nanocages (P-N-C/HNC), and porous fibers comprising PS nanobeads only (P-N-C) were also prepared under similar conditions.

2.3. Material characterization

A phase analysis of the as-prepared P-N-C@TiO_2/HNC and other composite NFs was performed using Bruker X-ray diffraction (D8) instrument at the Korea Basic Science Institute (Daegu). The morphological characteristics of the composite NFs were determined using field-emission scanning electron microscopy (FE-SEM) (UltraPlus; Zeiss) and field-emission transmission electron microscopy (JEM-2100F; JEOL). The thermal stability of the NFs was determined using thermogravimetric analysis (TGA) (Pyrsis 1; PerkinElmer) from room temperature to 800 °C, under a N_2 atmosphere at a ramping rate of 10 °C min^{-1}, unless stated otherwise. The chemical and bonding environments of the various elements in the as-prepared fibers were determined using X-ray photoelectron spectroscopy (XPS) (K-Alpha; Thermo Scientific) equipped with an Al Kα radiation source. N_2 adsorption–desorption isotherms were used to determine the specific surface area and pore size distribution of the as-prepared fibers based on the Brunauer–Emmett–Teller (BET) method using a surface analyzer. The crystallinity of the carbonaceous products in the as-prepared fibers was analyzed using Raman spectroscopy (LabRam, HR800, Horiba Jobin-Yvon).

2.4. Cell assembly and electrochemical measurements

Regular sulfur electrodes were prepared using a slurry-casting method by mixing elemental sulfur, super-P, and polyvinylidene fluoride (PVDF) binder in a weight ratio of 7:2:1 in *N*-methyl-2-pyrrolidone (NMP). The slurry was coated onto an aluminum current collector using a doctor blade and subsequently dried overnight at 60 °C. Thereafter, circular discs (φ = 14 mm) were punched and used as the working electrodes. The mass of sulfur in the electrodes was maintained at 2.52 mg (active-material loading of 1.64 mg cm^{-2}) throughout the electrochemical process. The coated separator as a multifunctional interlayer was also fabricated using a technique similar to that described above. Briefly, the as-prepared composite nanofibers (as the active material), super-P (as a conductive agent), and PVDF binder were thoroughly ground in a weight ratio of 7:2:1 dispersed overnight in NMP followed by coating on a commercial polypropylene separator and finally dried at 60 °C to evaporate the solvent. The circular discs (φ = 19 mm) were used as the interlayer and punched with an ultra-low areal loading of 0.19 mg cm^{-2}. Even with the additional cell components at the cathode side, the total sulfur content remained as high as 60.7 wt%. CR2032 coin cells were assembled using the working electrode as the cathode, Li metal as the anode, and a coated separator as a functional interlayer with the coated side facing toward the sulfur electrode. The electrolyte used was 1.0 M lithium bis(trifluoromethanesulfonyl)imide in a blend of 1,3-dioxolane (DOL) and 1,2-dimethoxyethane (DME) (1:1, v/v) with 0.5 M $LiNO_3$ as an additive. The total volume of the electrolyte inside the cells was fixed at 50 μL. The Li–S cells utilizing different interlayer arrangements were charged–discharged at various current rates ranging from 0.1 C to 0.5 C (1 C = 1675 mA h g^{-1}). The long-term cycling stability of the assembled Li–S cells constructed with different interlayer arrangements was evaluated at 0.1 C. Cyclic voltammetry measurements were performed at different voltage scan rates in the range of 0.05–0.5 mV s^{-1}. All electrochemical tests were performed using a WBCS3000 (WonATech) battery cycler at room temperature in a voltage window of 1.7–2.8 V. Nyquist plots were obtained using an electrochemical impedance analyzer (ZIVE SP2; WonATech) in the frequency range of 0.01 Hz–1 MHz with a 5 mV AC pulse.

2.5. Polysulfide adsorption and electrocatalytic activity tests

Visual polysulfide adsorption tests were also conducted to observe the polysulfide anchoring capability of the as-prepared nanostructures.

Briefly, Li_2S (≥99%, Sigma-Aldrich) and elemental sulfur powder (S; 99.98%, Sigma-Aldrich) were mixed in a weight ratio of 5:1 in DOL/DME solvent (1:1, v/v) to obtain a light-yellow Li_2S_6 polysulfide solution. A 1.0 mM solution of Li_2S_6 prepared in an appropriate amount of DOL/DME was added to three glass vials containing the as-prepared samples (3.0 mg). A pristine polysulfide solution was also prepared as a reference. To observe the catalytic effect of the as-prepared samples, symmetrical cells were assembled using a polysulfide solution and identical working counter electrodes (prepared using the slurry-casting method) separated by a Celgard 2400 membrane. The assembled cells were subjected to CV in the voltage range of −1.0 to 1.0 V, at a scan rate of 3.0 mV s^{-1}.

3. Results and discussion

The hierarchically porous graphitic C nanofibers comprising well-grafted TiO_2 quantum dots and ZIF-8 derived hollow N-doped C nanocages (P-N-C@TiO_2/HNC) were prepared using an electrospinning method. The detailed formation mechanism is shown in Scheme 1. The as-spun fibers comprise the homogeneous dispersion of TTIP, ZIF-8 polyhedrons (φ = 60 nm), and PS nanobeads (φ = 40 nm) in the PVP matrix, as shown in Scheme 1-①, and were stabilized overnight in a preheated oven at 150 °C to obtain the PVP/TTIP/PS/ZIF-8 composite fibers. The fibers were then heat-treated at 800 °C for 5 h under a N_2 atmosphere. During carbonization, PVP matrix was transformed into C products, whereas TTIP was converted into uniformly distributed titanium monoxide (TiO) quantum dots that were well grafted inside the C matrix (Scheme 1-②). In addition, the selective conversion of the C products into graphitic C (GC) and amorphous C (AC) occurs depending on the vicinity of the TiO quantum dots owing to their catalytic nature. Moreover, the ZIF-8 polyhedrons split into highly volatile Zn/Zn^{2+} species and N-rich organic ligands. During the heat treatment step, the volatile metal species evaporate, leaving behind highly ordered mesopores in the form of hollow nanocages, whereas the organic ligands are transformed into the N-doped C skeleton (Scheme 1-②). The detailed structural transformation of the ZIF-8 polyhedrons during the high-temperature heating step is shown in Scheme S1. Moreover, the PS nanobeads were completely removed at 800 °C, leaving pores inside the C framework (Scheme 1-②). This synergy between the PS nanobeads and ZIF-8 polyhedrons results in a highly porous N-C skeleton with open mesopores, which act as highly interconnected nanocages. The second heat-treatment step was performed at 300 °C for 3 h under an air atmosphere, which primarily resulted in the phase conversion of TiO to TiO_2, in addition to the selective decomposition of AC to CO_2 gas (Scheme 1-③). Overall, this synthetic methodology results in a highly porous N-doped GC skeleton that comprises well-grafted TiO_2 quantum dots accompanied by uniformly distributed interconnected HNCs that not only guarantee sufficient space for efficient electrolyte infiltration or electrode wetting but also accommodate the undesired volume variation (Scheme 1-④). In addition, the highly polar and homogeneously dispersed TiO_2 quantum dots prohibit the migration of sulfur-like species toward the anode thus increasing the active-material utilization and, hence enhancing the electrochemical performance.

The formation mechanism was further validated upon systematically

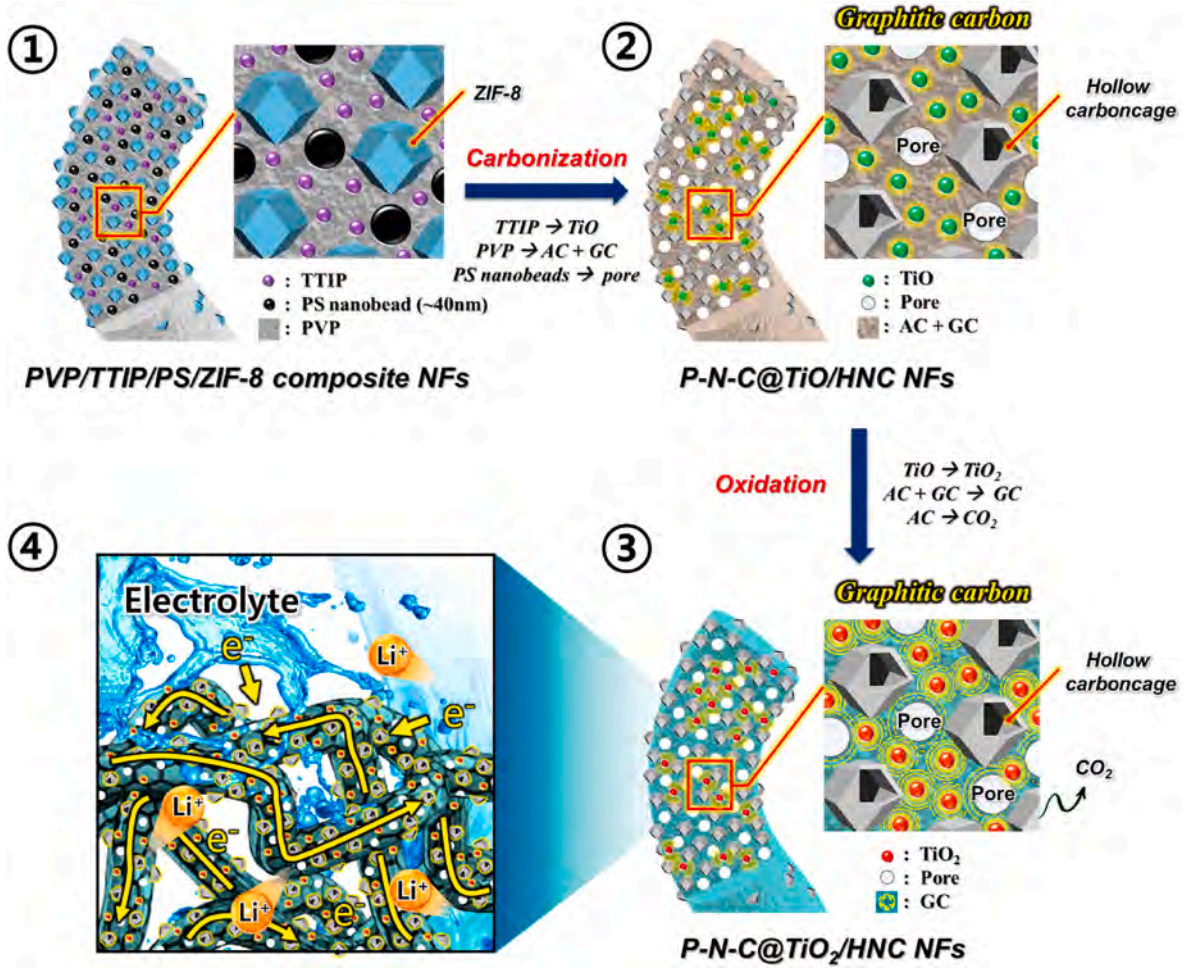

Scheme 1. Formation mechanism (①-④) of hierarchical porous nitrogen-doped carbon fibers comprising well-grafted TiO_2 quantum dots and ZIF-8 derived hollow carbon nanocage by electrospinning and subsequent heat-treatments as a coating interlayer for Li–S batteries.

examining the morphological and crystal structure changes of the as-prepared fibers after each synthesis step. The as-spun PVP/TTIP/PS/ZIF-8 composite nanofibers obtained after stabilization at 150 °C are shown in Fig. 1. The FE-SEM image (Fig. 1a) indicates the formation of continuous 1D fibrous morphology with a mean diameter of *ca.* 2.0 μm. In addition, the rough surface of the fibers was also apparent due to the uniform distribution of the ZIF-8 polyhedrons (φ = 60 nm) and PS nanobeads (φ = 40 nm) in the PVP matrix (Fig. 1b). The cross-sectional image shown in Fig. 1b also confirms the uniform distribution of the different constituents inside the nanofiber envelope. The XRD pattern obtained for the fibers shown in Fig. 1c exhibit well-resolved and intense peaks that can be primarily indexed to the ZIF-8 polyhedrons, which was in accordance with the XRD pattern of the as-prepared ZIF-8 polyhedrons (Fig. S1c). The characteristics of the as-prepared ZIF-8 polyhedrons are shown in Fig. S1. Furthermore, the thermal decomposition of the stabilized fibers is analyzed using TGA, as shown in Fig. 1d. The curve indicates a slight initial weight loss up to 100 °C owing to the loss of crystal water from the fibers. Afterward, the subsequent weight loss within the temperature range of 260 and 350 °C was attributed to the conversion of the PVP matrix to the carbonaceous products. Subsequently, the final steep weight loss to 580 °C corresponds to the decomposition of the PS nanobeads into gaseous products, whereas the PVP matrix continues to convert into carbonaceous products. In addition, the splitting of ZIF-8 polyhedrons into volatile Zn/Zn^{2+} species and N-rich organic units also contributes to the weight loss. The volatile metal species evaporate, whereas the organic units are converted into HNCs. Thereafter, no appreciable weight loss was observed up to 800 °C, suggesting the high thermal stability of the composite fibers. Therefore, we chose 800 °C as the optimal heat-treatment temperature to obtain the hierarchically porous composite fibers.

The as-spun PVP/TTIP/PS/ZIF-8 composite fibers were initially heat-treated at 800 °C under an N_2 atmosphere for 5 h, to obtain hierarchically porous N-doped C (P-N-C) NFs comprising well-grafted TiO quantum dots and HNCs (abbreviated as P-N-C@TiO/HNC), as shown in Fig. 2. The FE-SEM image in Fig. 2a shows that the fibrous structure of the as-spun fibers is maintained with numerous interconnected pores distributed homogeneously throughout the fiber length. This observation is also apparent from the high-resolution FE-SEM and cross-sectional images shown in Fig. 2b and c, respectively, which indicate the presence of open mesopores in the structure. The mesoporous structure was attributed to the successive conversion of the ZIF-8 polyhedrons into hollow C nanocages and the complete decomposition of the PS nanobeads in the composite. During the heat-treatment step, the organic groups in ZIF-8 are converted into N-doped C products, whereas the highly volatile reduced Zn species evaporate, leaving uniformly dispersed hollow nanocages (HNC) surrounded by N–C walls. The HNCs thus formed acts as reservoirs to store electrolyte that subsequently supports fast redox reactions inside the cell in a more efficient way besides inducing porosity to the nanostructure. In addition, the PS nanobeads (φ = 40 nm) were decomposed into gaseous products, resulting in additional porosity within the structure, which is beneficial for an efficient electrolyte penetration and the alleviation of the volume variation during the charge–discharge process [1]. Similarly, PVP also converts into the N-doped C matrix, and the titanium salt is reduced into TiO quantum dots, which are well-grafted inside the N–C scaffold. These observations are well supported by the TEM images shown in Fig. 2d and

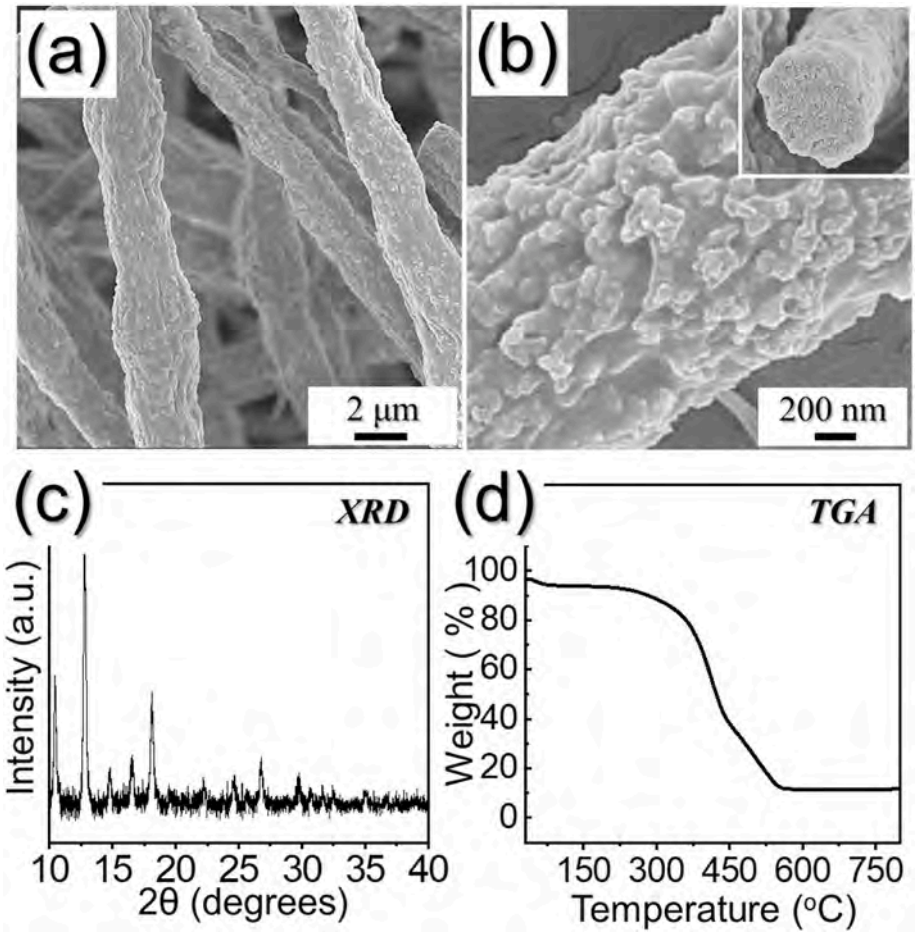

Fig. 1. Physical characterization of as-spun PVP/TTIP/PS/ZIF-8 composite fibers obtained after stabilization at 150 °C: (a, b) FE-SEM images and in inset is the cross-sectional image, (c) XRD pattern, and (d) TG curve in N_2 atmosphere.

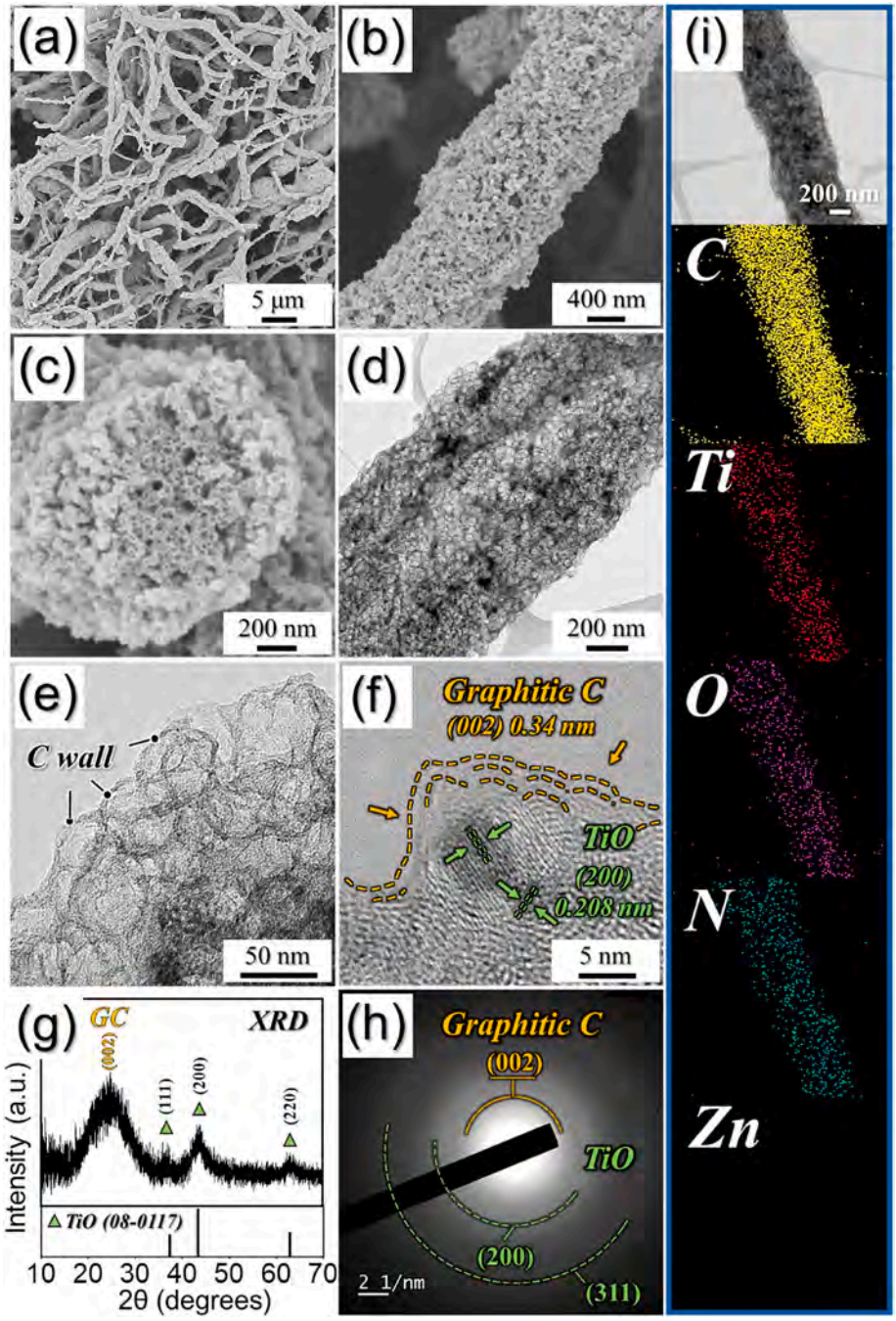

Fig. 2. Characterization of P-N-C@TiO/HNC fibers obtained after the first heat-treatment of stabilized composite fibers at 800 °C in N_2 atmosphere: (a, b) FE-SEM images, (c) cross-sectional image, (d, e) TEM images, (f) HR-TEM image, (g) XRD pattern, (h) SAED pattern, and (i) elemental mapping images.

e, which confirm the presence of bright regions associated with the hollow C nanocages and the gray and dark regions correspond to the GC and TiO quantum dots, respectively. The hollow N–C nanocages with a mean diameter of ~50 nm in the fibrous nanostructure are more apparent in Fig. 2e and are surrounded by a carbon wall with a thickness of ~5 nm. Furthermore, the HR-TEM image shown in Fig. 2f indicates the presence of the well-embedded TiO quantum dots with diameters of 5 nm inside the N–C skeleton with a fairly distinct lattice fringe spacing of 0.208 nm, which corresponds to the (200) crystal plane. Moreover, the lattice fringe spacing of 0.34 nm was assigned to the (002) plane of the GC. The XRD pattern shown in Fig. 2g exhibits diffraction peaks associated with GC ($2\theta = 25°$) and the TiO nanocrystalline phase. The selected area electron diffraction pattern (SAED) shown in Fig. 2h exhibits diffraction rings that correspond to the GC and TiO crystal phase, which are in good agreement with the XRD results. The elemental dot mapping images presented in Fig. 2i indicate the homogeneous dispersion of carbon, titanium, oxygen, and nitrogen in the 1D fibrous nanostructure. In addition, no traces of zinc were observed, suggesting the complete removal of the Zn/Zn^{2+} species from the structure.

The hierarchically porous C fibers comprising well-grafted TiO_2 quantum dots and hollow N-doped C nanocages inside the N-C scaffold (P-N-C@TiO_2/HNC) were finally obtained after the second heat-treatment step at 300 °C in air, as shown in Fig. 3. The FE-SEM images shown in Fig. 3a suggest that the fibrous morphology was maintained after the heat-treatment step. In addition, the porous structure was well preserved (Fig. 3b and c). The TEM image in Fig. 3d exhibits

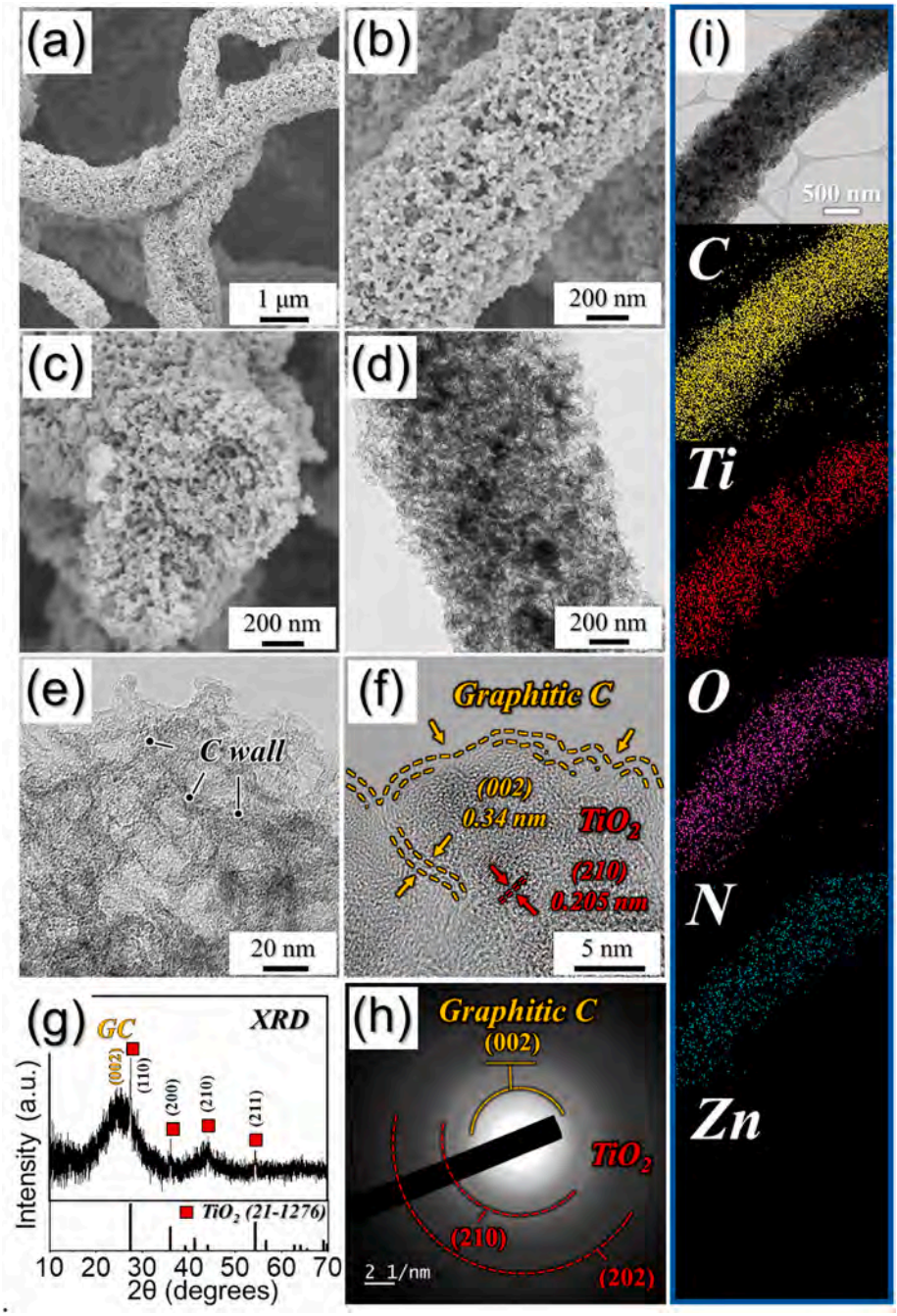

Fig. 3. Morphologies, SAED, XRD pattern, and elemental mapping images of the P-N-C@TiO_2/HNC composite fibers obtained after second heat-treatment at 300 °C in an air atmosphere: (a, b) FE-SEM images, (c) cross-sectional image, (d, e) TEM images, (f) HR-TEM image, (g) XRD pattern, (h) SAED pattern, and (i) elemental mapping images.

similar fibrous morphologies with bright, gray, and dark regions corresponding to the hollow nanocages, GC, and TiO_2 quantum dots, respectively, which are well confined within the carbon scaffold. During oxidation, the TiO crystal phase was converted into the TiO_2 phase. Moreover, the AC with a low decomposition temperature in the carbon matrix was selectively removed from the composite, leaving only residual GC. Therefore, the removal of AC forms additional pores in the structure. The robustness of the nanostructure was also evident from the high-magnification TEM image (Fig. 3e), indicating the homogeneous presence of hollow N–C nanocages in the nanostructure. The HR-TEM image shown in Fig. 3f suggests well-embedded nanocrystalline TiO_2 quantum dots with lattice fringes separated by a distance of 0.205 nm corresponding to the (210) lattice plane. In addition, the lattice fringe of separation 0.34 nm corresponding to the (002) plane of GC was also evident. The XRD pattern in Fig. 3g shows diffraction peaks that can be assigned to the GC and TiO_2 crystalline phases, which suggest the complete phase conversion of TiO into TiO_2. The SAED pattern in Fig. 3h also confirms the diffraction rings associated with the GC and TiO_2 crystal phases. Moreover, the uniform dispersion of various elements such as carbon, titanium, oxygen, and nitrogen in the elemental mapping images (Fig. 3i) indicates the presence of TiO_2 nanocrystals inside the N-doped C framework. Overall, the formation of a hierarchically porous N-doped C framework comprising well-trapped TiO_2 quantum dots and uniformly distributed hollow N–C nanocages was verified.

The chemical environment and bonding state of the various elements in the as-prepared P-N-C@TiO_2/HNC nanofibers are analyzed using

XPS, as shown in Fig. 4. The XPS survey spectrum shown in Fig. 4a exhibits well-distinguished photoelectron peaks corresponding to the C 1s, N 1s, Ti 2p, and O 1s orbitals in the as-prepared nanofibers. The high-resolution Ti 2p XPS spectrum in Fig. 4b shows two fitted peaks at binding energies of 458.0 (Ti $2p_{3/2}$) and 463.8 (Ti $2p_{1/2}$) eV, which can be assigned to the Ti^{4+} species [43–45]. Moreover, the binding energy separation between the two intense peaks ($\Delta E = 5.8$ eV) was consistent with that previously reported [46]. Moreover, the two low intense peaks centered at binding energies of 461.3 and 456.0 eV were assigned to the Ti^{3+} (Ti_2O_3) valence state due to the partial incomplete oxidation of Ti [47,48]. However, their low intensity suggests that the proportion of Ti_2O_3 in the as-prepared sample was almost insignificant. The deconvoluted O 1s spectrum shown in Fig. 4c exhibits three closely spaced photoelectron peaks at binding energies of 531.2, 532.9, and 534.1 eV, which correspond to the Ti–O, –OH, and O–C bonds, respectively [49,50]. The C 1s high-resolution XPS profile shown in Fig. 4d exhibits four well-fitted peaks at binding energies of 284.5, 285.2, 287.2, and 288.4 eV, which can be assigned to the –C=C–, –C–N/C–C–, –C–O–, and –C=O– bonds, respectively, and match well with that previously reported [51–54]. The presence of a highly intense –C=C– peak firmly confirms the presence of carbonaceous species in the as-prepared fibers. In addition, the –C–N/C–C– peaks indicate N-doping in the carbonaceous framework [1,16]. N-doping generally results in a high electronic conductivity due to the increased electronegative nature of the N atom, when compared to C. To validate this, the deconvoluted N 1s XPS spectrum is obtained, as shown in Fig. 4e, which exhibits three distinct peaks at 398.2, 400.0, and 403.7 eV corresponding to pyridinic N, pyrrolic N, and graphitic N, respectively, and firmly confirm the N-doping in the C framework [16,53]. An elemental analysis is performed to quantify the N content in the composite, as shown in Table S1. The nitrogen content was observed to be 9.7 wt% in the structure and primarily induced from the N-rich organic units in the PVP polymer and

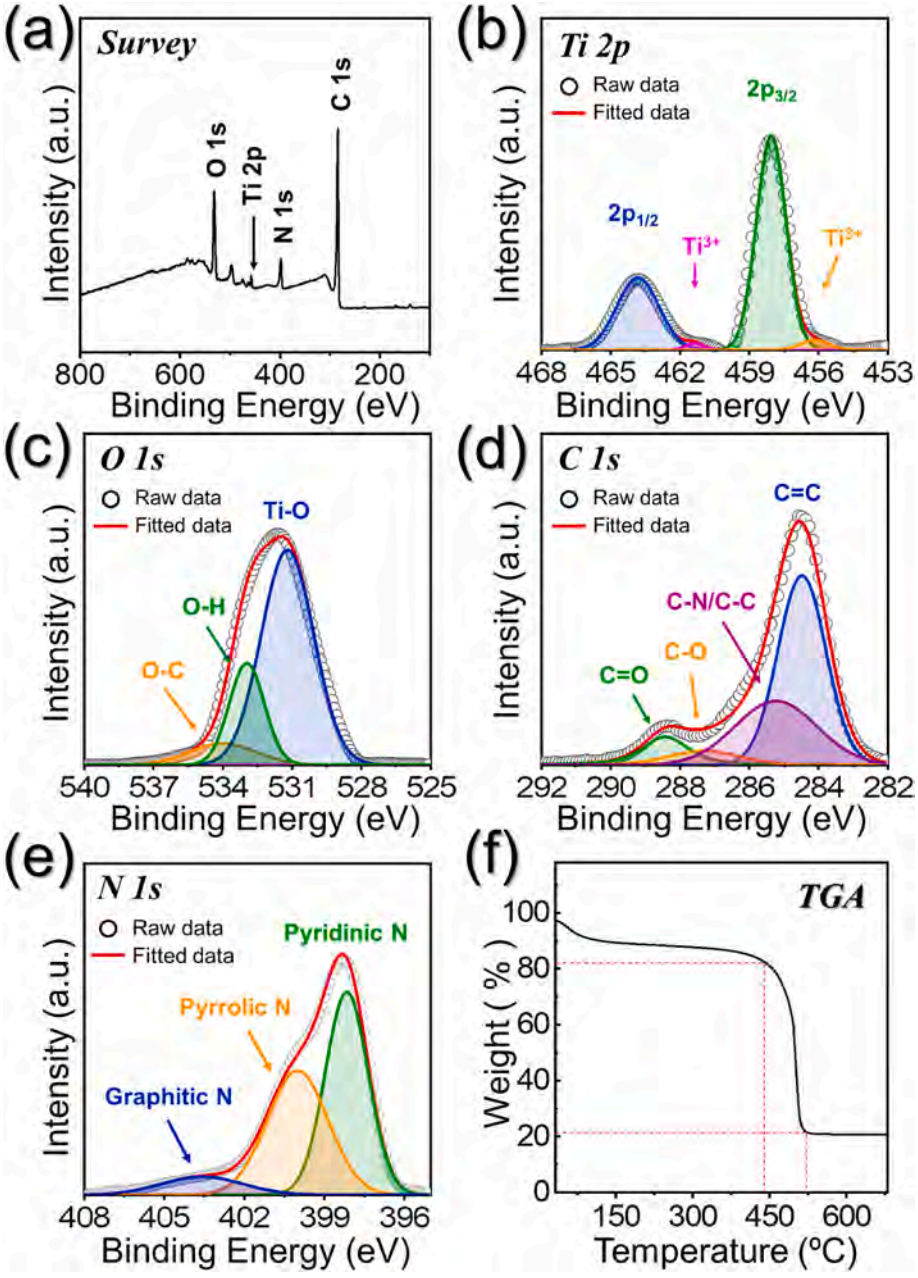

Fig. 4. (a) XPS survey spectrum, (b) Ti 2p XPS spectrum, (c) O 1s XPS spectrum, (d) C 1s XPS spectrum, (e) N 1s XPS spectrum, and (f) TG curve of P-N-C@TiO_2/HNC fibers.

ZIF-8 polyhedrons precursors. In addition, TGA under an air atmosphere is performed to quantify the carbon and TiO_2 content, as shown in Fig. 4f, which indicates the presence of 68 wt% carbon and 20 wt% TiO_2. Furthermore, Raman spectroscopy is performed to examine the crystalline nature of the carbonaceous products in the P-N-C@TiO_2/HNC sample, as shown in Fig. S2b. To observe the changes in the carbonaceous materials in a better manner, the composite nanofiber sample prior to oxidation (P-N-C@TiO/HNC) was also analyzed (Fig. S2a). Both samples display a typical Raman signature with D- and G-bands centered at 1350 and 1600 cm^{-1}, respectively. However, the relative intensity ratio of the two bands, i.e., I_D/I_G, which is usually considered as a crucial parameter to examine the crystallinity of carbon products, differs significantly for the two samples [55]. For instance, the I_D/I_G ratio prior to oxidation was 1.26, indicating that the carbon material inside the sample was primarily amorphous, whereas after oxidation, the I_D/I_G ratio decreased to 0.87, indicating the selective removal of the AC under the air atmosphere. However, a lower I_D/I_G ratio also indicates a lower degree of defects or disordered arrangement in the as-prepared sample, which subsequently affects the porosity of the sample. To validate this observation, adsorption–desorption isotherms are obtained for the as-prepared nanofibers before and after oxidation using N_2 as the adsorbate gas, as shown in Figs. S3a–d. The pre-oxidized sample (P-N-C@TiO/HNC) exhibits a high BET surface area of 673 $m^2\ g^{-1}$ (Fig. S3a), primarily originating from the mesopores in the nanostructure, as evident from the type IV isotherm curve. In addition, the pore-size distribution curve shown in Fig. S3b confirms the presence of mesopores with a peak centered at 42 nm. However, the P-N-C@TiO_2/HNC composite nanofibers display a slightly lower surface area (612 $m^2\ g^{-1}$) with a mesopore peak located at 15 nm after oxidation. This can be attributed to the burning of the porous AC in the nanostructure during the oxidation step. These observations are consistent with the Raman results discussed earlier. Therefore, it is quite clear that the P-N-C@TiO_2/HNC composite nanofibers mostly consist of N-doped carbonaceous products comprising well-embedded TiO_2 quantum dots and uniformly distributed N-doped hollow carbon nanocages.

To verify the structural merits of the P-N-C@TiO_2/HNC composite NFs, a spinning solution for comparison sample i.e., without TTIP (PVP/PS/ZIF-8) was also prepared along with PVP/PS (i.e., without TTIP and ZIF-8). The as-spun PVP/PS/ZIF-8 composite fibers stabilized at 150 °C indicate a continuous fibrous morphology with a mean diameter of ~1.5 μm (Fig. S4a). The composite fibers after the heat treatment at 800 °C were abbreviated as P-N-C/HNC and are shown in Fig. S5. The FE-SEM images in Figs. S5a–c indicates 1D fibrous morphology (mean diameter ~1.0 μm) along with the uniform distribution of the hollow nanocages with open pores all over the structure. The XRD pattern (Fig. S5g) also confirms that the nanostructure completely consists of carbonaceous material. The SAED pattern with a diffuse diffraction ring (Fig. S5h) was in good accordance with the XRD results, which corresponds to AC only. The elemental mapping results (Fig. S5i) suggests that carbon and nitrogen were evenly dispersed throughout the nanofibers. Moreover, no traces of zinc are observed, indicating the complete removal of Zn/Zn^{2+} species, which results in the highly porous nanostructure. An extremely high surface area of 1019 $m^2\ g^{-1}$ (Fig. S6a) is observed due to the formation of mesopores with an average pore diameter of 30 nm, as shown in Fig. S6b. Similarly, the morphology and phase analysis results of the porous nanofibers (P-N-C) obtained after heat treatment of the stabilized PVP/PS composite fibers (Fig. S7) are shown in Figs. S8a–e, respectively, along with the corresponding discussion.

Before analyzing the electrochemical performance of the Li–S cells utilizing different coating separator arrangements, the physical properties of the separator coatings are analyzed, as shown in Fig. S9. A digital photograph of the coated separator shown in Fig. S9a reveals the crack-free and uniform coating formed over a commercial Celgard 2400 separator. In addition, the coating thickness (~26 μm) appears to be uniform for all of the separator arrangements, as shown in Figs. S9b–e. Moreover, the coated separator exhibits a high mechanical integrity even upon bending and twisting, as shown in Fig. S9f. In addition, all of the utilized separators are highly uniform in the measured dimensions (φ = 19 mm), as shown in Fig. S9g. Furthermore, the surfaces of the pristine and coated separators along with the coating cross-section are observed using FE-SEM, as shown in Figs. S10a–c. The surfaces of the pristine and uncoated separators (Fig. S10a) reveal a nanometer-sized opening for a smooth diffusion of the charged species during the redox processes. In contrast, the surface of the coated separator reveals a uniform deposition of the as-prepared nanofibers (Fig. S10b). The thickness of the coated layer was ~30 μm as observed from the cross-sectional FE-SEM image shown in Fig. S10c and is consistent with the thickness measurements results in Fig. S9.

The electrochemical performances of various Li–S cells employing different coated separators are shown in Fig. 5. The cells are initially subjected to CV in a voltage window of 1.7–2.8 V at a voltage scan rate of 0.1 mV s^{-1}, as shown in Fig. 5a and Figs. S11a–c. The CV curves display well-resolved cathodic and anodic peaks for all of the Li–S cells utilizing different coated separator arrangements. The first CV scans shown in Fig. 5a display two cathodic peaks centered at ~2.3 and ~2.0 V, which can be assigned to the successive reduction of elemental sulfur to lower-order lithium polysulfide (Li_2S_x; $3 \leq x \leq 1$) via intermediate higher order (Li_2S_x; $8 \leq x \leq 6$) and middle-order lithium polysulfide (Li_2S_x; $6 \leq x \leq 4$), respectively [16]. In addition, slightly broad anodic peaks observed at ~2.4 V suggest the effective conversion of low-order discharge products to elemental sulfur via intermediate polysulfides, thus completing the cycle [7]. However, a clear difference in the current intensities suggests a difference in the specific discharge capacity values. In addition, the CV curves for the first five initial cycles for Li–S cells utilizing the different coating arrangements shown in Fig. S11 display almost overlapping profiles, suggesting the highly reversible electrochemical processes occurring inside of the cells. To confirm the CV results, the Li–S cells with different coated separator arrangements are subjected to the charge–discharge process at 0.1 C (1C = 1675 mA h g^{-1}), as shown in Fig. 5b. The Li–S cells employing P-N-C@TiO_2/HNC, P-N-C/HNC, and P-N-C NFs as the coated interlayer display initial discharge capacities of 1377, 1089, and 903 mA h g^{-1}, respectively. In addition, clear charge–discharge plateaus suggest typical redox reactions involving elemental sulfur and its discharge product (Li_2S), that are consistent with the CV results. Moreover, the high upper (Q_H) and lower (Q_L) discharge capacity values observed for the Li–S cell utilizing the P-N-C@TiO_2/HNC coated separator suggests an efficient trapping and reuse of the sulfur-like species. The obtained capacity values seem reasonably high when considering the high effective sulfur content in the cathode region (~61 wt%). This was attributed to the presence of well-grafted TiO_2 quantum dots that act as chemical adsorption sites for capturing polysulfide species, restricting their migration toward the anode and result in high active-material utilization. Moreover, the availability of the highly conductive N–C skeleton ensures enormous conductive channels for the rapid transfer of charged species, which in turn guarantee kinetically favored redox processes. These observations are in good agreement with the potential polarization values calculated for all of the assembled cells. The Li–S cell employing P-N-C@TiO_2/HNC displays the lowest polarization potential (ΔV = 260 mV) when compared to the Li–S cell utilizing P-N-C/HNC (ΔV = 290 mV) and P-N-C (ΔV = 300 mV). Therefore, CV and initial charge–discharge results show the overall enhanced electrochemical performance of the P-N-C@TiO_2/HNC NFs compared to the other prepared nanostructures owing to the synergetic effects of the highly conductive and porous N–C scaffold, as well as the availability of numerous adsorption sites.

The Li–S cells utilizing various coated separator arrangements are further subjected to rate capability tests at various C-rates ranging from 0.1 to 0.5C, as shown in Fig. 5c. The Li–S cells utilizing P-N-C@TiO_2/HNC NFs as coated functional interlayers display initial discharge capacities of 1377, 976, 846, and 742 mA h g^{-1} at 0.1, 0.2, 0.3, and 0.5C,

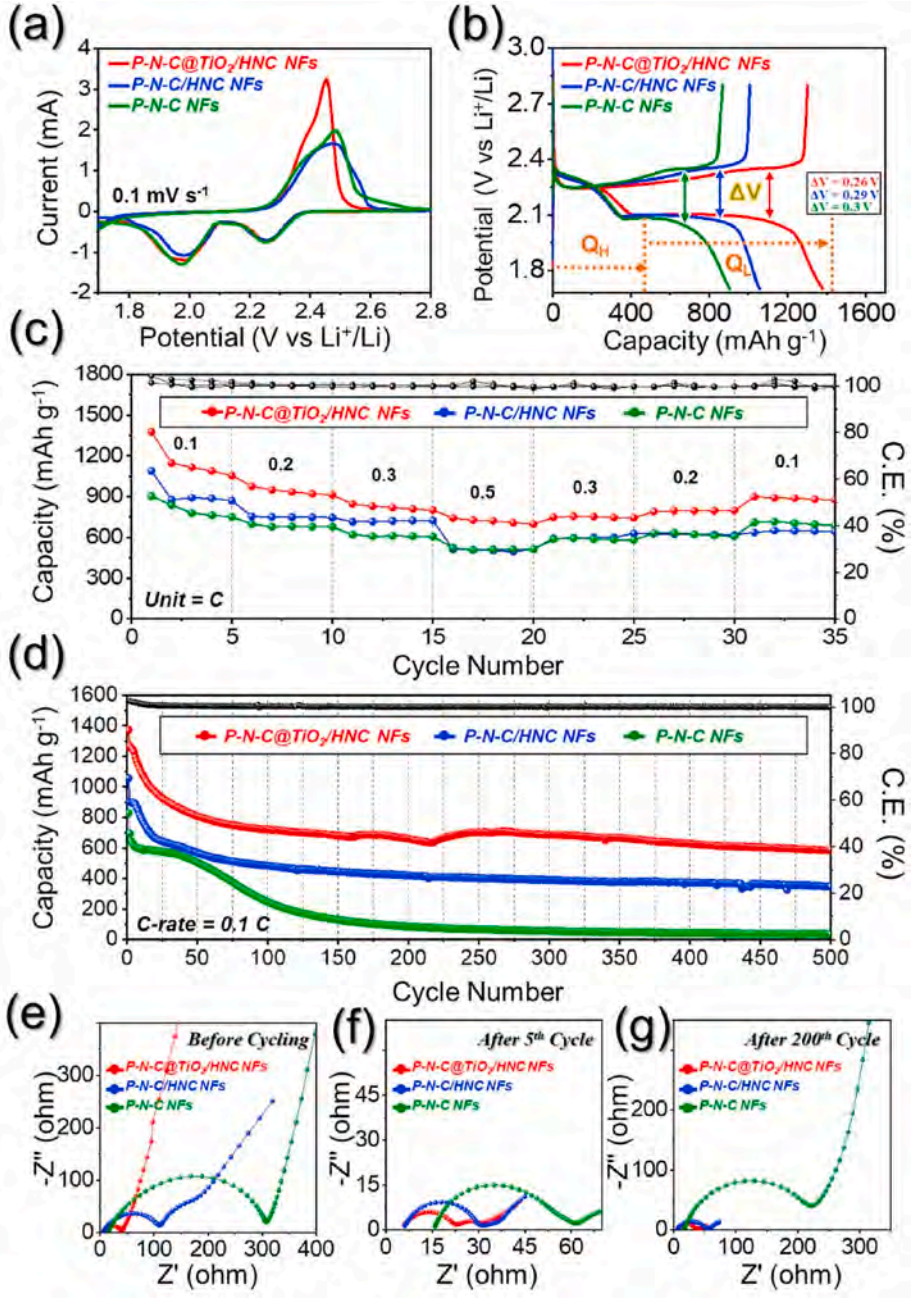

Fig. 5. (a–d) Electrochemical performances and (e–g) Nyquist impedance plots of Li–S cells assembled with different interlayer arrangements: (a) initial CV curves at 0.1 mV s^{-1}, (b) initial charge–discharge voltage profiles at 0.1 C-rate, (c) rate capability test, (d) cycling performance of the assembled cells at 0.1 C-rate, and Nyquist plots at different cycle number: (e) before cycling, (f) after the 5th cycle, and (g) after 200th cycle.

respectively. In contrast, the Li–S cell employing the P-N-C/HNC and P-N-C NF-coated separator display lower discharge capacities of 1089/903, 754/698, 715/620, and 514/523 mA h g^{-1}, respectively, at identical C-rates, suggesting the superior structural advantages of the P-N-C@TiO_2/HNC NFs. Moreover, the discharge capacity values obtained for the P-N-C@TiO_2/HNC NF-coated separator seem overwhelming considering the high effective sulfur content in the cathode region (~61 wt%). Furthermore, when the current was reversed, the Li–S cell employing the P-N-C@TiO_2/HNC NF-coated separator recovers 65% (898 mA h g^{-1}) of the initial capacity at 0.1C. These results are primarily due to the highly conductive N–C framework that supports the fast redox kinetics via rapid charge transfer, highly porous structure for efficient electrolyte infiltration, and availability of polar species in the form of TiO_2 quantum dots that guarantee the effective anchoring of lithium polysulfide species and restricts their migration toward the anode, which enhances the active-material utilization. These observations are well supported by the well-developed charge–discharge profiles with long voltage plateaus (Fig. S12a) observed for P-N-C@TiO_2/HNC when compared with the other Li–S cells. In addition, the capacity utilization curves are plotted and analyzed for all of the Li–S cells, as shown in Fig. S13, which again suggest that the P-N-C@TiO_2/HNC coated separator exhibits the highest active-material utilization at all C-rates studied, suggesting the fast redox kinetics inside the cell. Even at a C-rate of 0.5C, the P-N-C@TiO_2/HNC-coated separator cell displays a capacity utilization of 44%. Besides, the Li–S cell utilizing P-N-C@TiO_2/HNC also exhibit reasonable high-rate capability performance, as shown in Fig. S14.

The assembled Li–S cells were further subjected to long-term cycling

stability tests at 0.1C, as shown in Fig. 5d. The Li–S cell employing the P-N-C@TiO_2/HNC-coated separator as the functional interlayer exhibits an initial discharge capacity of 1373 mA h g^{-1} (81% of the theoretical value), which reduces monotonically to 723 mA h g^{-1} at the 100th cycle. However, upon further cycling, the capacity seems to be highly stable with a final value of 590 mA h g^{-1} (~43% capacity retention) observed at the end of the 500th cycle with an average capacity decay rate of only 0.11% per cycle. However, the significant capacity augment during cycling process could be attributed to the activation of the trapped sulfur species. Such activation process generally beneficial for the long-term cycling performance as it can compensate the active material loss during the cycling. Additionally, a slightly above 100% Coulombic efficiency is primarily due to the infinite Li-source (anode) compared to the sulfur cathode. Besides, it also confirms that the highly reversible redox processes occurring inside the Li–S cell. In contrast, the Li–S cells employing the P-N-C/HNC NF-coated separator interlayer also displays a similar trend, but the capacity decay process was much more pronounced. For instance, the Li–S cell displays an initial discharge capacity of 1058 mA h g^{-1} (63% of the theoretical capacity), which constantly decreases and finally stabilizes at 348 mA h g^{-1} (~33% capacity retention) at the end of the 500th cycle with an average capacity decay of 0.13% per cycle. Similarly, the separator coated with P-N-C NFs also displays poor cycling stability with an initial discharge capacity of 828 mA h g^{-1} (49% of the theoretical capacity), which reduces sharply to 36 mA h g^{-1} (~4% capacity retention) at the end of the 500th cycle with an average capacity decay rate of 0.19% per cycle. The poor cycling stability of the P-N-C/HNC and P-N-C NF-coated separator was attributed to the non-availability of numerous chemisorption sites in the form of polar material that efficiently capture the polysulfide species and restrict the active-material loss. These results are further verified by considering the respective charge–discharge profiles of the different Li–S cells utilizing various coated separator arrangements at various cycle numbers, as shown in Fig. S15. Overall, the cycling results further confirm that the structural advantages in P-N-C@TiO_2/HNC not only allow fast redox kinetics owing to the efficient diffusion of charge species but also effectively absorb unwanted volume variations in addition to an efficient polysulfide trapping. Furthermore, the electrochemical performance of Li-S cell employing high sulfur loading electrodes and low E/S ratio were also explored, as shown in Fig. S16. The electrolyte volume was fixed at 30 μL for high loading Li-S cells. As a result, a low E/S ratio of 9.7 (for 2.0 mg cm^{-2}) and 6.5 μL mg^{-1} (for 3.0 mg cm^{-2}) was obtained. The Li-S cell employing high loading electrodes exhibit stable cycling performance at 0.1 C-rate with a discharge capacity of 823 (for 2.0 mg cm^{-2}) and 747 (for 3.0 mg cm^{-2}) mA h g^{-1} at the end of 45th cycle. These results again confirm the structural merits of the P-N-C@TiO_2/HNC NFs.

The enhanced reaction kinetics inside the Li–S cells are confirmed using Nyquist plot analysis, as shown in Fig. 5e–g. The equivalent circuit fitting model along with the impedance parameters for various Li–S cells featuring different coated separator arrangements are listed in Fig. S17 and Table S2, respectively. The impedance was measured for all of the freshly assembled cells at an open-circuit voltage, as well as at different cycle numbers in a fully charge state during cycling at 0.1 C. The solution resistance (R_s) corresponding to the Li–S cells featuring the P-N-C@TiO_2/HNC- and P-N-C/HNC NF-coated separator displays the lowest, similar values, even after the 200th continuous charge–discharge cycle, suggesting a highly stable electrode–separator–electrolyte interface. In contrast, the assembled Li–S cells utilizing the P-N-C NF-coated separator display slightly higher R_s values, implying that the redox processes at the interface are relatively slow. Furthermore, the Li–S cell employing the P-N-C@TiO_2/HNC NF-coated separator displays the lowest charge transfer resistance (R_{ct}) throughout the cycling study when compared to the other Li–S cells. For instance, after the 200th cycle, the Li–S cell employing P-N-C@TiO_2/HNC-NF-coated separator exhibits an R_{ct} of 27.8 Ω compared to 48.2 and 207.5 Ω observed for the Li–S cells prepared using the P-N-C/HNC and P-N-C-NF-coated separators, respectively. These results suggest that the structural merits of P-N-C@TiO_2/HNC NFs not only ensure a kinetically favored redox process inside the Li–S cell but also enhance the integrity of the electrode during prolonged cycling.

To further validate the redox kinetics inside the cells, the Li-ion diffusion coefficient (D_{Li}^+) is calculated using CV measurements performed at different voltage scan rates from 0.05 to 0.5 mV s^{-1} in a voltage window of 1.7–2.8 V, as shown in Fig. 6. The CV plots obtained at different scan rates display typical Li–S redox peaks, implying that the reaction processes are between elemental sulfur and its discharge product (Li_2S). However, the high current intensity observed for the Li–S cell employing P-N-C@TiO_2/HNC NFs, even at a higher voltage scan rate of 0.5 mV s^{-1} compared to the other Li–S cells, suggest fast redox processes combined with an enhanced diffusion of charge species. The Randles–Sevcik equation was used to further quantify the D_{Li}^+ values as follows [16]:

$$I_p = 2.69 \times 10^5 \, n^{1.5} \, A \, D_{Li}{}^{+0.5} \, C_{Li} \, v^{0.5} \quad (1)$$

where I_p is the redox peak current, n is the number of electrons involved in the reaction ($n = 2$), A is the electrode surface area (cm^2), C_{Li} is the Li-ion concentration (mol L^{-1}), and v is the voltage scan rate (V s^{-1}). The I_p vs. $v^{0.5}$ curves obtained for the Li–S cells featuring the P-N-C@TiO_2/HNC-, P-N-C/HNC-, and P-N-C-NF-coated separators are shown in Fig. 6 and their corresponding D_{Li}^+ values calculated for the Li–S cells are summarized in Table S3. The Li–S cell featuring P-N-C@TiO_2/HNC displays the highest diffusion coefficient values for all three redox peaks when compared to the other Li–S cells, suggesting the superior diffusion processes inside the cell. This again validates the structural superiority of the P-N-C@TiO_2/HNC NFs when compared to the other samples in enhancing their overall electrochemical performance.

To elucidate the catalytic conversion of lithium polysulfide by the P-N-C@TiO_2/HNC NF-coated separator, we analyze the CV curves using symmetrical cells employing the as-prepared nanofibers as the counter and working electrodes infiltrated with the prepared catholyte solution, as shown in Fig. 7. The first CV profiles obtained at a scan rate of 3 mV s^{-1} in the voltage window of −1.0 to 1.0 V for all of the assembled symmetrical cells are shown in Fig. 7a. The CV plots display appreciable differences with the P-N-C@TiO_2/HNC NF symmetrical cell exhibiting an efficient catalytic behavior toward lithium polysulfides, as evident from the high current intensity peaks. In contrast, the symmetrical cell utilizing the P-N-C/HNC electrodes displays relatively low catalytic effects toward polysulfides due to the non-polar nature of the as-prepared NFs. Similarly, the symmetrical cell featuring the P-N-C NF electrode exhibits the lowest polysulfide catalytic conversion effect, as evident from the low current values. In addition, the CV curves for five successive cycles of all the symmetric cells shown in Fig. 7b–d display exact overlapping profiles, implying an effective catalytic conversion, although to different extents. These observations are further validated using visual polysulfide adsorption tests, as shown in Fig. 7e. A clear adsorption of the polysulfide solution was evident from the as-prepared P-N-C@TiO_2/HNC NFs with a continuous change in color from yellow (at t = 0) to transparent (t = 1 h). In contrast, the polysulfide solution added to P-N-C/HNC and P-N-C NFs display polysulfide adsorption due to the N-doped C framework, but to a lower extent, as evident from the light-yellow color of the solution even after 1 h. A schematic illustration of the P-N-C@TiO_2/HNC NFs as a functional interlayer restricting the migration of lithium polysulfides from diffusing toward the Li anode is shown in Fig. 7f. These results again confirm that the structural advantages of the P-N-C@TiO_2/HNC NFs resulted in the efficient trapping/reuse of the lithium polysulfide species due to the presence of well-grafted TiO_2 quantum dots. Furthermore, the post-cycling morphologies presented in Fig. S18 firmly authenticates the above results. The FE-SEM image of the coated separator utilizing P-N-C@TiO_2/HNC NFs (Fig. S18a) implies that the fibrous structure remains intact even after the prolonged cycling thus indicating high structural integrity of the

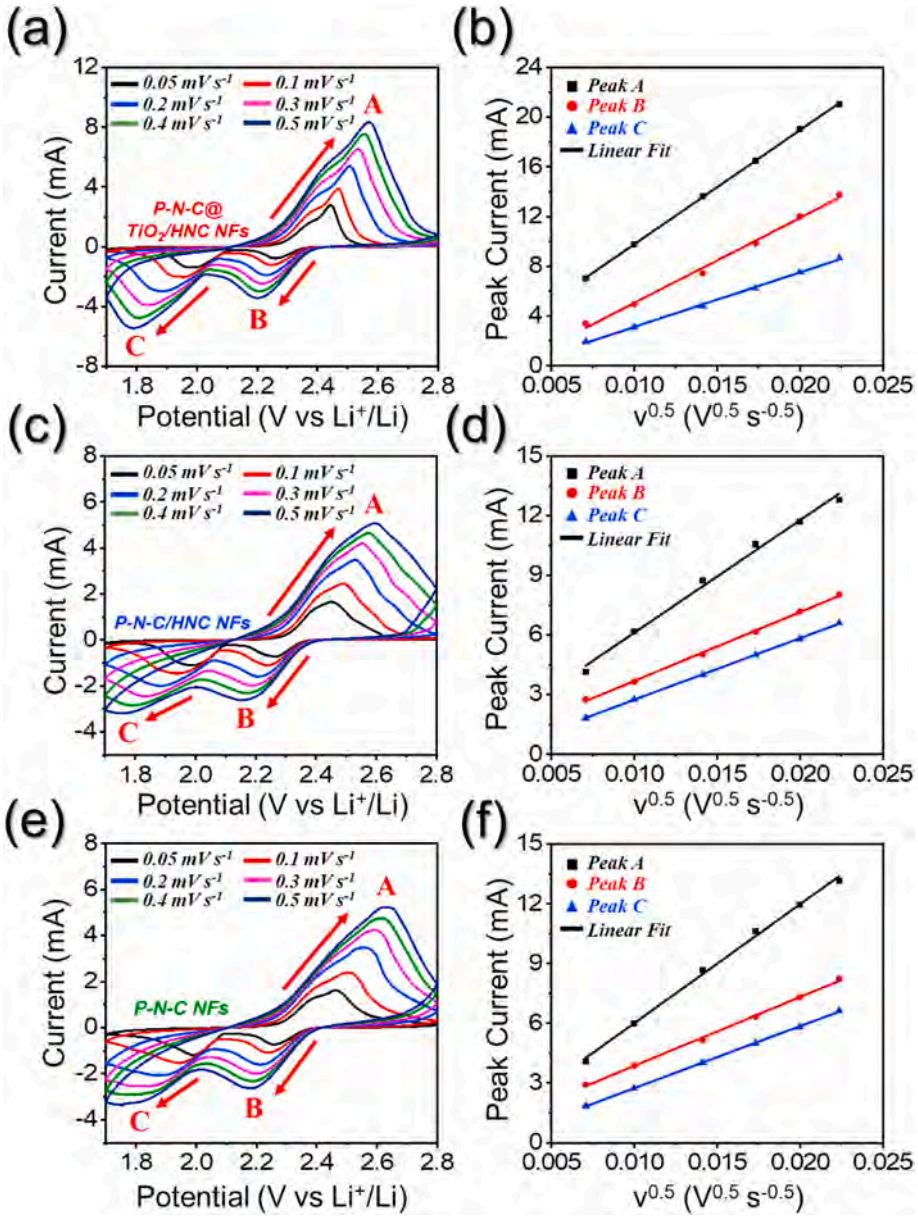

Fig. 6. Lithium-ion diffusion coefficient (D_{Li+}) for the assembled Li–S cells with different coated separators: (a, b) P-N-C@TiO_2/HNC NFs, (c, d) P-N-C/HNC NFs, and (e, f) P-N-C NFs.

nanostructure. Besides, no polysulfide deposits were observed suggesting effective catalytic conversion of the sulfur-like species (as indicated by the color of the separator in an opened cell). In contrast, the cells employing P-N-C/HNC NFs (Fig. S18b) and P-N-C NFs (Fig. S18c) coated separator display large polysulfide deposits indicating poor catalytic conversion effect due to absence of redox-active species also evident from the digital images of the opened cells.

Overall, the incorporation of a highly porous, conductive, and ultralightweight functional interlayer in the form of P-N-C@TiO_2/HNC NFs inserted on the cathode side of a commercial Celgard separator result in an overall improved electrochemical performance with a reasonable rate capability and stable prolonged cycling. The results are highly promising considering the high effective sulfur content (~61 wt%) in the cathode region and can be attributed to the synergetic effects of hierarchically porous and highly conductive N–C framework that provide numerous conductive channels for rapid charge transfer along with the efficient electrolyte percolation. In addition, the presence of polar TiO_2 quantum dots ensures an efficient trapping and reuse of the lithium polysulfide species, leading to high active-material utilization. Therefore, we believe that the present strategy will provide substantial insight into the synthesis of hierarchical porous and conductive nanostructures suitable for various rechargeable applications.

4. Conclusions

In summary, we have carried out a detailed investigation of the synergetic effects of incorporating a multifunctional interlayer at the cathode side to restrict the migration of lithium polysulfide toward the anode, to improve the overall electrochemical performance. The interlayer consists of a hierarchically porous and highly conductive N–C skeleton for fast redox reactions and well-grafted TiO_2 quantum dots for efficient polysulfide anchoring. The assembled Li–S cell utilizing a highly effective sulfur cathode and P-N-C@TiO_2/HNC-coated separator as a multifunctional interlayer exhibited an overall improved electrochemical performance with a satisfactory rate capability and stable long-term stability (500 cycles at 0.1 C). The nanostructure design strategy

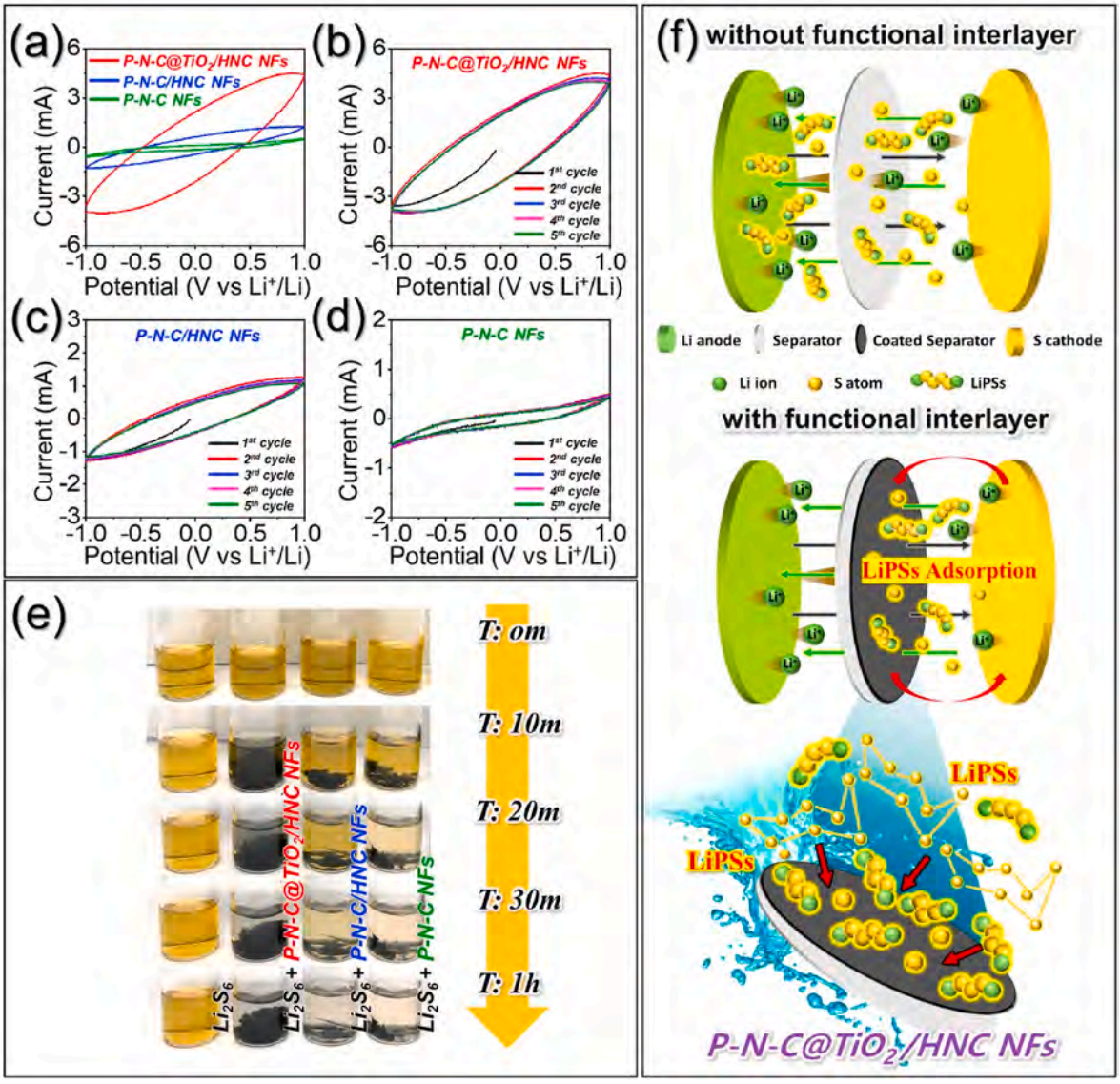

Fig. 7. (a) First CV profile of different symmetric cells in the voltage window of −1.0 to 1.0 V at a scan rate of 3.0 mV s^{-1}, (b–d) First five CV curves obtained using different symmetric cells arrangements, (e) Digital photographs of visual demonstration of polysulfide adsorption tests, and (f) schematic illustration of utilizing P-N-C@TiO_2/HNC NFs as a functional interlayer for prohibiting lithium polysulfide migration.

discussed in the present work will provide insights toward the development of advanced functional materials as interlayers for a wide range of energy storage applications.

Authors contribution

Young Hoe Seon designed the idea, performed experiments, and write the manuscript. **Rakesh Saroha** performed experiments, and write the manuscript. **Jung Sang Cho** supervise the work along with writing-review and editing.

Declaration of competing interest

The authors declare that they have no known competing financial interests or personal relationships that could have appeared to influence the work reported in this paper.

Acknowledgements

Funding: This work was supported by the National Research Foundation of Korea (NRF), funded by the Korean government (MSIP) [grant numbers: NRF-2021R1A4A2001687 and NRF-2021R1I1A3057700].

Appendix A. Supplementary data

Supplementary data to this article can be found online at https://doi.org/10.1016/j.compositesb.2022.109856.

References

[1] Saroha R, Oh JH, Seon YH, Kang YC, Lee JS, Cho JS. Freestanding interlayers for Li–S batteries: design and synthesis of hierarchically porous N-doped C nanofibers comprising vanadium nitride quantum dots and MOF-derived hollow N-doped C nanocages. J Mater Chem 2021;9:11651–64.
[2] Nulu A, Nulu V, Sohn KY. Silicon and porous MWCNT composite as high capacity anode for lithium-ion batteries. Kor J Chem Eng 2020;37(10):1795–802.
[3] Chung S-H, Manthiram A. High-performance Li–S batteries with an ultra-lightweight MWCNT-coated separator. J Phys Chem Lett 2014;5(11):1978–83.
[4] Belgibayeva A, Taniguchi I. Insights into the improved electrochemical performance of lithium–sulfur battery with free-standing SiO_2/C composite nanofiber mat interlayer. J Power Sources 2021;484:229308.

[5] Fan Q, Liu W, Weng Z, Sun Y, Wang H. Ternary hybrid material for high-performance lithium–sulfur battery. J Am Chem Soc 2015;137(40):12946–53.
[6] Pu X, Yang G, Yu C. Trapping polysulfides catholyte in carbon nanofiber sponges for improving the performances of sulfur batteries. J Electrochem Soc 2015;162(7):A1396.
[7] Saroha R, Heo J, Li X, Angulakshmi N, Lee Y, Ahn H-J, et al. Asymmetric separator integrated with ferroelectric-$BaTiO_3$ and mesoporous-CNT for the reutilization of soluble polysulfide in lithium-sulfur batteries. J Alloys Compd 2022;893:162272.
[8] Saroha R, Heo J, Liu Y, Angulakshmi N, Lee Y, Cho K-K, et al. V_2O_3-decorated carbon nanofibers as a robust interlayer for long-lived, high-performance, room-temperature sodium–sulfur batteries. Chem Eng J 2022;431:134205.
[9] Wang J, Xiao K, Ouyang B, Zhang L, Yang H, Liu J, et al. Simultaneous immobilization and conversion of polysulfides on Co_3O_4–CoN heterostructured mediators toward high-performance lithium–sulfur batteries. ACS Appl Energy Mater 2019;2(4):2570–8.
[10] Jiang Y, Liu H, Tan X, Guo L, Zhang J, Liu S, et al. Monoclinic ZIF-8 nanosheet-derived 2D carbon nanosheets as sulfur immobilizer for high-performance lithium sulfur batteries. ACS Appl Mater Interfaces 2017;9(30):25239–49.
[11] Liang G, Wu J, Qin X, Liu M, Li Q, He Y-B, et al. Ultrafine TiO_2 decorated carbon nanofibers as multifunctional interlayer for high-performance lithium–sulfur battery. ACS Appl Mater Interfaces 2016;8(35):23105–13.
[12] Saroha R, Cho JS. Nanofibers comprising interconnected chain-like hollow N-doped C nanocages as 3D free-standing cathodes for Li–S batteries with super-high sulfur content and lean electrolyte/sulfur ratio. Small Methods 2022:2200049.
[13] Li S, Jin B, Zhai X, Li H, Jiang Q. Review of carbon materials for lithium-sulfur batteries. ChemistrySelect 2018;3(8):2245–60.
[14] Xu Z-L, Kim J-K, Kang K. Carbon nanomaterials for advanced lithium sulfur batteries. Nano Today 2018;19:84–107.
[15] Saroha R, Ahn J-H, Cho JS. A short review on dissolved lithium polysulfide catholytes for advanced lithium-sulfur batteries. Kor J Chem Eng 2021;38:461–74.
[16] Saroha R, Oh JH, Lee JS, Kang YC, Jeong SM, Kang D-W, et al. Hierarchically porous nanofibers comprising multiple core–shell Co_3O_4@graphitic carbon nanoparticles grafted within N-doped CNTs as functional interlayers for excellent Li–S batteries. Chem Eng J 2021;426:130805.
[17] Kumar D, Rajouria SK, Kuhar SB, Kanchan D. Progress and prospects of sodium-sulfur batteries: a review. Solid State Ionics 2017;312:8–16.
[18] Deng Z-f, Zhang Z-a, Hai L, Lai Y-q, Jin L, Jie L, et al. Vapor-grown carbon fibers enhanced sulfur-multi walled carbon nanotubes composite cathode for lithium/sulfur batteries. T Nonferr Metal Soc 2014;24(1):158–63.
[19] Lu S, Chen Y, Wu X, Wang Z, Li Y. Three-dimensional sulfur/graphene multifunctional hybrid sponges for lithium-sulfur batteries with large areal mass loading. Sci Rep 2014;4(1):1–4.
[20] Zhou G, Paek E, Hwang GS, Manthiram A. Long-life Li/polysulphide batteries with high sulphur loading enabled by lightweight three-dimensional nitrogen/sulphur-codoped graphene sponge. Nat Commun 2015;6(1):1–11.
[21] Jin F, Xiao S, Lu L, Wang Y. Efficient activation of high-loading sulfur by small CNTs confined inside a large CNT for high-capacity and high-rate lithium–sulfur batteries. Nano Lett 2015;16(1):440–7.
[22] Li G, Lei W, Luo D, Deng Y, Deng Z, Wang D, et al. Stringed "tube on cube" nanohybrids as compact cathode matrix for high-loading and lean-electrolyte lithium–sulfur batteries. Energy Environ Sci 2018;11(9):2372–81.
[23] Sun Z, Guo Y, Li B, Tan T, Zhao Y. ZnO/carbon nanotube/reduced graphene oxide composite film as an effective interlayer for lithium/sulfur batteries. Solid State Sci 2019;95:105924.
[24] Zhu L, Li C, Ren W, Qin M, Xu L. Multifunctional vanadium nitride@ N-doped carbon composites for kinetically enhanced lithium–sulfur batteries. New J Chem 2018;42(7):5109–16.
[25] Sun Z, Zhang J, Yin L, Hu G, Fang R, Cheng H-M, et al. Conductive porous vanadium nitride/graphene composite as chemical anchor of polysulfides for lithium-sulfur batteries. Nat Commun 2017;8(1):1–8.
[26] Moorthy B, Kwon S, Kim J-H, Ragupathy P, Lee HM, Kim DK. Tin sulfide modified separator as an efficient polysulfide trapper for stable cycling performance in Li–S batteries. Nanoscale Horiz 2019;4(1):214–22.
[27] Zhou Z, Li Y, Fang T, Zhao Y, Wang Q, Zhang J, et al. MOF-Derived Co_3O_4 polyhedrons as efficient polysulfides barrier on polyimide separators for high temperature lithium–sulfur batteries. Nanomaterials 2019;9(11):1574.
[28] Zhou G, Zhao Y, Zu C, Manthiram A. Free-standing TiO_2 nanowire-embedded graphene hybrid membrane for advanced Li/dissolved polysulfide batteries. Nano Energy 2015;12:240–9.
[29] Xue W, Yan Q-B, Xu G, Suo L, Chen Y, Wang C, et al. Double-oxide sulfur host for advanced lithium-sulfur batteries. Nano Energy 2017;38:12–8.
[30] Lim E, Chun J, Jo C, Hwang J. Recent advances in the synthesis of mesoporous materials and their application to lithium-ion batteries and hybrid supercapacitors. Kor J Chem Eng 2021;38:227–47.
[31] Guo Y, Li J, Pitcheri R, Zhu J, Wen P, Qiu Y. Electrospun Ti_4O_7/C conductive nanofibers as interlayer for lithium-sulfur batteries with ultra long cycle life and high-rate capability. Chem Eng J 2019;355:390–8.
[32] Liu Y, Li G, Fu J, Chen Z, Peng X. Strings of porous carbon polyhedrons as self-standing cathode host for high-energy-density lithium–sulfur batteries. Angew Chem Int Ed 2017;129(22):6272–6.
[33] Zhang Y, Zhang X, Silva SRP, Ding B, Zhang P, Shao G. Lithium–sulfur batteries meet electrospinning: recent advances and the key parameters for high gravimetric and volume energy density. Adv Sci 2021:2103879.
[34] Shi Z, Sun Z, Cai J, Yang X, Wei C, Wang M, et al. Manipulating electrocatalytic Li_2S redox via selective dual-defect engineering for Li–S batteries. Adv Mater 2021;33(43):2103050.
[35] Shi Z, Li M, Sun J, Chen Z. Defect engineering for expediting Li–S chemistry: strategies, mechanisms, and perspectives. Adv Energy Mater 2021;11(23):2100332.
[36] Li Z, Zhou C, Hua J, Hong X, Sun C, Li HW, et al. Engineering oxygen vacancies in a polysulfide-blocking layer with enhanced catalytic ability. Adv Mater 2020;32(10):1907444.
[37] Zhao C-X, Li X-Y, Zhao M, Chen Z-X, Song Y-W, Chen W-J, et al. Semi-immobilized molecular electrocatalysts for high-performance lithium–sulfur batteries. J Am Chem Soc 2021;143(47):19865–72.
[38] Wang Q, Jin J, Wu X, Ma G, Yang J, Wen Z. A shuttle effect free lithium sulfur battery based on a hybrid electrolyte. Phys Chem Chem Phys 2014;16(39):21225–9.
[39] Qu C, Chen Y, Yang X, Zhang H, Li X, Zhang H. $LiNO_3$-free electrolyte for Li–S battery: a solvent of choice with low Ksp of polysulfide and low dendrite of lithium. Nano Energy 2017;39:262–72.
[40] Ma G, Wen Z, Wu M, Shen C, Wang Q, Jin J, et al. A lithium anode protection guided highly-stable lithium–sulfur battery. Chem Commun 2014;50(91):14209–12.
[41] Wang Y, Sahadeo E, Rubloff G, Lin C-F, Lee SB. High-capacity lithium sulfur battery and beyond: a review of metal anode protection layers and perspective of solid-state electrolytes. J Mater Sci 2019;54(5):3671–93.
[42] Jo MS, Ghosh S, Jeong SM, Kang YC, Cho JS. Coral-like yolk–shell-structured nickel oxide/carbon composite microspheres for high-performance Li-ion storage anodes. Nano-Micro Lett 2019;11(1):1–18.
[43] Peng W-C, Chen Y-C, He J-L, Ou S-L, Horng R-H, Wuu D-S. Tunability of p-and n-channel TiO_x thin film transistors. Sci Rep 2018;8(1):1–11.
[44] Kitchamsetti N, Kalubarme RS, Chikate PR, Park CJ, Ma YR, Shirage PM, et al. An investigation on the effect of Li–ion ccling on the vertically aligned brookite TiO_2 nanostructure. ChemistrySelect 2019;4(21):6620–6.
[45] Nguyen HH, Gyawali G, Martinez-Oviedo A, Nguyen HP, Lee SW. Modified blue TiO_2 nanostructures for efficient photo-oxidative removal of harmful NO_x gases. Kor J Chem Eng 2020;37(9):1507–14.
[46] Biesinger MC, Payne BP, Grosvenor AP, Lau LW, Gerson AR, Smart RSC. Resolving surface chemical states in XPS analysis of first row transition metals, oxides and hydroxides: Cr, Mn, Fe, Co and Ni. Appl Surf Sci 2011;257(7):2717–30.
[47] Xie W, Li R, Xu Q. Enhanced photocatalytic activity of Se-doped TiO_2 under visible light irradiation. Sci Rep 2018;8(1):1–10.
[48] Hierro-Oliva M, Gallardo-Moreno A, González-Martín M. XPS analysis of Ti_6Al_4V oxidation under UHV conditions. Metall Mater Trans 2014;45(13):6285–90.
[49] Wang Q, Xie D, Chen J, Liu G, Yu M. Superhydrophobic paper fabricated via nanostructured titanium dioxide-functionalized wood cellulose fibers. J Mater Sci 2020;55(16):7084–94.
[50] Gong S, Jiang Z, Zhu S, Fan J, Xu Q, Min Y. The synthesis of graphene-TiO_2/gC_3N_4 super-thin heterojunctions with enhanced visible-light photocatalytic activities. J Nanoparticle Res 2018;20(11):1–13.
[51] Jo MS, Lee JS, Jeong SY, Kim JK, Kang YC, Kang DW, et al. Golden bristlegrass-like hierarchical graphene nanofibers entangled with N-Doped CNTs containing $CoSe_2$ nanocrystals at each node as anodes for high-rate sodium-ion batteries. Small 2020;16(38):2003391.
[52] Lee JS, Jo MS, Saroha R, Jung DS, Seon YH, Lee JS, et al. Hierarchically well-developed porous graphene nanofibers comprising N-Doped graphitic C-coated cobalt oxide hollow nanospheres as anodes for high-rate Li-ion batteries. Small 2020;16:2002213.
[53] Lee JS, Saroha R, Oh SH, Shin DH, Jeong SM, Kim JK, et al. Rational Design of perforated bimetallic (Ni, Mo) sulfides/N-doped graphitic carbon composite microspheres as anode materials for superior Na-ion batteries. Small Methods 2021;5:2100195.
[54] Oh SH, Park SM, Kang D-W, Kang YC, Cho JS. Fibrous network of highly integrated carbon nanotubes/MoO_3 composite bundles anchored with MoO_3 nanoplates for superior lithium ion battery anodes. J Ind Eng Chem 2020;83:438–48.
[55] Saroha R, Panwar AK. Effect of in situ pyrolysis of acetylene (C_2H_2) gas as a carbon source on the electrochemical performance of $LiFePO_4$ for rechargeable lithium-ion batteries. J Phys D 2017;50(25):255501.